Concurrent Mapping and Localization Using Sidescan Sonar

Ioseba Tena Ruiz, *Member, IEEE*, Sébastien de Raucourt, Yvan Petillot, *Member, IEEE*, and David M. Lane, *Member, IEEE*

***Abstract*—This paper describes and evaluates a concurrent mapping and localization (CML) algorithm suitable for localizing an autonomous underwater vehicle. The proposed CML algorithm uses a sidescan sonar to sense the environment. The returns from the sonar are used to detect landmarks in the vehicle's vicinity. These landmarks are used, in conjunction with a vehicle model, by the CML algorithm to concurrently build an absolute map of the environment and to localize the vehicle in absolute coordinates. As the vehicle moves forward, the areas covered by a forward-look sonar overlap, whereas little or no overlap occurs when using sidescan sonar. It has been demonstrated that numerous reobservations by a forward-look sonar of the landmarks can be used to perform CML. Multipass missions, such as sets of parallel and regularly spaced linear tracks, allow a few reobservations of each landmark with sidescan sonar. An evaluation of the CML algorithm using sidescan sonar is made on this type of trajectory. The estimated trajectory provided by the CML algorithm shows significant jerks in the positions and heading brought about by the corrections that occur when a landmark is reobserved. Thus, this trajectory is not useful to mosaic the sea bed. This paper proposes the implementation of an optimal smoother on the CML solution. A forward stochastic map is used in conjunction with a backward Rauch–Tung–Striebel filter to provide the smoothed trajectory. This paper presents simulation and real results and shows that the smoothed CML solution helps to produce a more accurate navigation solution and a smooth navigation trajectory. This paper also shows that the qualitative value of the mosaics produced using CML is far superior to those that do not use it.**

***Index Terms*—Concurrent mapping and localization, mosaics, sidescan sonar, smoothing.**

I. Introduction

THE ADVENT of autonomous underwater vehicles (AUVs) has posed a number of new challenges to the robotics research community. Among these challenges, the question of true autonomy remains unresolved. Autonomy can be defined as the ability to provide for oneself without the help of others. Unmanned underwater vehicles (UUVs), be they AUVs or remotely operated vehicles (ROVs), are not yet capable of navigating without receiving position fixes from either a global positioning system (GPS) or acoustic transponders. They are not genuinely autonomous in the navigation sense. Navigation itself poses three distinct questions: "*where am I?*", "*where am I going?*", and "*how should I get there?*" [1]. This paper will focus on the first of these questions.

Most UUVs are equipped with *dead-reckoning sensors*, such as a Doppler velocity log (DVL) and inertial rate gyros or magnetic compasses [2]–[5]. These types of sensors suffer from drift; thus, the error in the vehicle's position will grow without bounds. To fix the position of the vehicle on the world frame, *absolute-positioning* sensors are used. Commercial absolute-positioning sensors adapted to the underwater environment include acoustic positioning systems; such as super short, short, and long baseline (LBL) navigation. Currently, the state of the art in applied inertial navigation for small UUVs includes support from DVL as well as acoustic short- and long-baseline navigation systems [5]. All of these systems require the vehicle to be within a volume of water that they cover, therefore restricting the vehicle's exploratory capabilities and not allowing for true autonomy. This has motivated the underwater navigation community to investigate and develop terrain-based navigation [6]–[10] and CML [11]–[14] systems.

Terrain-based navigation uses *a priori* known terrain characteristics to localize a vehicle through observations. The more recent CML concept builds a map of previously unknown landmarks and concurrently localizes the vehicle in the map [1], [15], [16]. Our chosen approach is the *stochastic map* proposed by Smith *et al.* [17]. The stochastic map is essentially an augmented extended Kalman filter (EKF). As a new landmark is observed, it is simply added into the state vector. Reobservations of landmarks provide state measurements and, thus, allow drift corrections. The sensor chosen to perform CML must allow perfect data associations and numerous reobservations of landmarks. If the observations are matched with the wrong landmarks, the stochastic map can break down. This paper assumes that the data association produces perfect matches and sidesteps this problem. For a discussion on the data-association process, refer to [18].

Given the task at hand, i.e., localizing an underwater vehicle, sonar is the most appropriate choice to sense the surroundings. Using a forward-look sonar allows multiple reobservations of a landmark, as shown in Fig. 1. The CML process relies on the reobservation of landmarks and past work used forward-look sonar. The effectiveness of CML using forward-look sonar and stochastic map has been demonstrated and much work has been already carried out on this subject, including demonstrations using real data [11], [18]–[20].

Sidescan sonars are downward looking and are not useful CML sensors for missions where only one pass of the sea floor is performed (Fig. 1). For multipass missions, such as sets of

Manuscript received February 7, 2003; revised March 12, 2004.

I. Tena Ruiz, Y. Petillot, and D. M. Lane are with the School of Engineering and Physical Sciences, Heriot-Watt University, Edinburgh EH14 4AS, U.K. (e-mail: I.Tena_Ruiz@hw.ac.uk; Y.R.Petillot@hw.ac.uk).

S. de Raucourt was with the School of Engineering and Physical Sciences, Heriot-Watt University, Edinburgh EH14 4AS, U.K.

Digital Object Identifier 10.1109/JOE.2004.829790

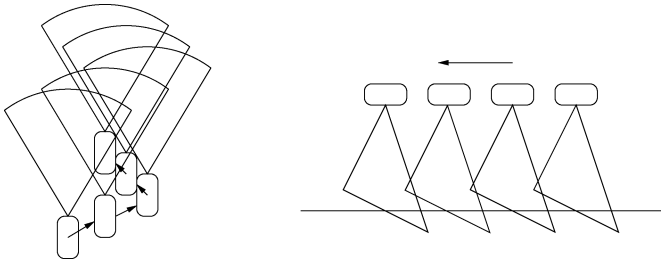

Fig. 1. Sidescan and forward-look sonar. As the vehicle moves forward, the regions covered by the forward-look sonar overlap (right). No overlap occurs when a sidescan sonar is used (left).

parallel and regularly spaced linear tracks where the separation between the parallel tracks in the trajectory is less than the sonar maximum range, these sensors might prove to be a useful ally. Sidescan sonars provide far higher quality images than forward-look sonars, which will help the data association. Parallel and regularly spaced linear tracks are commonly used in survey missions and sidescan sonars are an essential part of a survey AUV's payload. Their use for CML should, therefore, be considered seriously.

A great number of papers discussing image segmentation, classification, registration, and landmark extraction have already been published [21]–[26]. Data-association algorithms for CML have also received considerable attention [18], [20], [27]–[31]. Other papers address the issue of data association in the context of sonar images [32] and some address the issue of matching sidescan images [33]. High-quality images provided by sidescan sonar will help the data association process (see Fig. 2).

In most survey missions, a landmark on the sea bed is observed two or three times. The efficiency of CML with such a small amount of reobservations must be assessed. Section II will examine this process and evaluate the efficiency of the system.

Observations, by correcting the drift, create *jerks* in the estimation. Thus, trajectory estimation using conventional CML solutions remain unsuitable for some data exploitation techniques, such as georeferenced mosaicing. CML using sidescan sonar will require an appropriate smoothing postprocess. Postprocessing the navigation solution given by CML is examined in Section III. The final section will show mosaics obtained with real data, which show that the smoothed CML solution can be used to produce high quality coherent georeferenced images.

II. CML Using Sidescan Sonar

This section examines the use of CML using returns from a sidescan sonar and describes the stochastic map, a common and well-founded technique used to perform CML. This will be done in the first subsection. Section II-B will describe the implementation of CML techniques with a sidescan sonar. In Section II-C, a number of simulation experiments will be thoroughly examined. These experiments will demonstrate the usefulness of the stochastic map when using a sidescan sonar. The experiments will also compare the performance of a sidescan sonar system to a forward-look system.

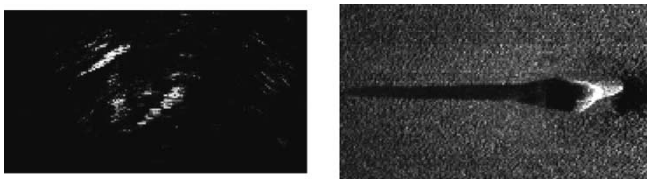

Fig. 2. Data association. These images of different targets show that (left) forward-look sonars provide poorer quality images and (right) sidescan sonars provide higher quality images. High-quality images will help the data-association task considerably.

A. Stochastic Map

The stochastic map is an augmented-state EKF [34], [35]. In this incarnation, the filter now holds the relevant states of the vehicle and those of the landmarks in a single-state vector. The advantage of this method is that it allows us to continually update and maintain the vehicle-to-vehicle, landmark-to-vehicle and landmark-to-landmark correlations. Recent research [36] has demonstrated the advantages obtained by maintaining these correlations. This research has motivated our choice of approach. Under this architecture, the state vector $\mathbf{x}$ assumes the form

$$\mathbf{x} = [\mathbf{x_v} \mathbf{x_1} \dots \mathbf{x_n}]' \tag{1}$$

where $'$ is the transpose of a vector or matrix, $\mathbf{x_v}$ holds the state of the vehicle and $\mathbf{x_1}, \dots, \mathbf{x_n}$ hold the state of the n landmarks. The estimated error covariance for this system,

$$\mathbf{P} = \begin{bmatrix} \mathbf{P_{vv}} & \mathbf{P_{v1}} & \dots & \mathbf{P_{vn}} \\ \mathbf{P_{1v}} & \mathbf{P_{11}} & \dots & \mathbf{P_{1n}} \\ \vdots & \vdots & \ddots & \vdots \\ \mathbf{P_{nv}} & \mathbf{P_{n1}} & \dots & \mathbf{P_{nn}} \end{bmatrix} \tag{2}$$

where the submatrices $\mathbf{P_{vv}}$, $\mathbf{P_{vi}}$, and $\mathbf{P_{ii}}$ are the vehicle-to-vehicle, vehicle-to-landmark, and landmark-to-landmark covariances, respectively.

The state and covariance are updated according to the EKF update equations. The stochastic map assumes fixed landmarks. Observations that were not associated to an existing landmark will be added to the stochastic map state and covariance as new landmark states.

The new map state vector will be

$$\mathbf{x} \leftarrow \begin{bmatrix} \mathbf{x} \\ \mathbf{x_{n+1}} \end{bmatrix} \tag{3}$$

where the position of the new landmark

$$\mathbf{x_{n+1}} = l[\mathbf{x_v}, \mathbf{z_{new}}]. \tag{4}$$

Here, l is the function that outputs the landmark state $\mathbf{x_{n+1}}$ with input parameters $\mathbf{x_v}$ and $\mathbf{z_{new}}$, the new observation vector. The new covariance and correlation terms will be

$$\begin{aligned} \mathbf{P_{n+1n+1}} &= \mathbf{L_v P_{vv} L_v'} + \mathbf{L_z R L_z'} \\ \mathbf{P_{n+1v}} &= \mathbf{P'_{vn+1}} = \mathbf{L_v P_{vv}} \\ \mathbf{P_{n+1i}} &= \mathbf{P'_{in+1}} = \mathbf{L_v P_{vi}} \end{aligned} \tag{5}$$

where $\mathbf{L_v}$ and $\mathbf{L_z}$ are the Jacobian of (4) with respect to the robot vehicle state $\mathbf{x_v}$, evaluated at $\hat{\mathbf{x}}_\mathbf{v}$, and to the new observa-

tion $\mathbf{z_{new}}$, evaluated at $\mathbf{z_{new}}$ and $\mathbf{R}$ is the measurement error covariance.

The problem associated with the stochastic map is that, as the number of landmarks increases, the computational burden increases in $O(N^3)$ time, where N is the number of states in the filter. This has motivated a number of research groups to decouple the filter, effectively ignoring the correlations. Some of these efforts have yielded good approximations of the full stochastic map. The most relevant of these are the *covariance intersection* [14], [31] and the *decoupled stochastic map* [13]. These efforts show promising results. However, they are approximations to the full map and some recent telling work shows that ignoring the correlations can be very much counterproductive [37]. An alternative approach is to keep the number of landmarks within a set limit [38]. This paper focuses on a postprocessing implementation and the actual processing requirements have not been considered.

B. Implementation

The stochastic map algorithm has been implemented to operate in a simulated environment with both types of sonar: sidescan and forward-look. A suitable vehicle model has also been implemented to estimate the position of a generic underwater vehicle. The models are detailed as follows.

a) Vehicle model: The dynamic model must be compatible with all kinds of vehicles (tow-fish, torpedo shape AUV, manipulation UV, ...). A centrilinear constant speed and constant yaw model fits these requirements and involves all the usually available data. More accurate dynamic models could have been chosen, but they are less flexible. The dynamic equations of the chosen model are

$$\begin{cases} x_{n+1} = x_n + v_n \sin\theta_n dt \\ y_{n+1} = y_n + v_n \cos\theta_n dt \\ v_{n+1} = v_n + \omega_v \\ \theta_{n+1} = \theta_n + \omega_\theta \end{cases} \tag{6}$$

where v denotes the speed, θ the heading with respect to the north (clockwise), (x, y) are the vehicle-position coordinates with respect to an east/north frame, and ω_v and ω_θ are zero-mean, white, and Gaussian process noise speed and heading errors.

This model has been found to yield accurate estimates for this kind of problem and, given a suitable update rate, no divergences due to nonlinearities have to be feared. The gap between the actual dynamics and the model must be represented in the process noise to allow convergence and correct estimation. The process noise must take the unknown yaw rate and acceleration into account.

b) Sonar observations: For a vehicle using a forward-look sonar, returning range, and angle with respect to the vehicle frame, the observation vector will be $\mathbf{z_i} = [r\ \psi]'$. Following this, the prediction for landmarks $\mathbf{x_i}$ will be

$$\hat{\mathbf{z}}_\mathbf{i} = \begin{bmatrix} \sqrt{\bar{x}_i^2 + \bar{y}_i^2} \\ \arctan(\bar{x}_i, \bar{y}_i) - \theta_v \end{bmatrix} \tag{7}$$

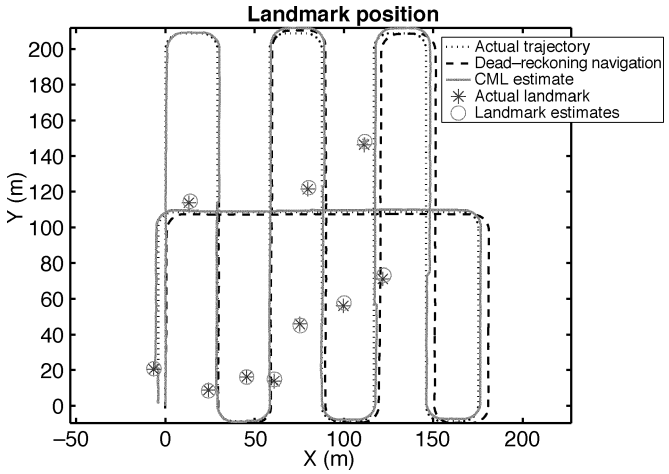

Fig. 3. Simulation results. The observations of the ten landmarks allow correction of the position estimate.

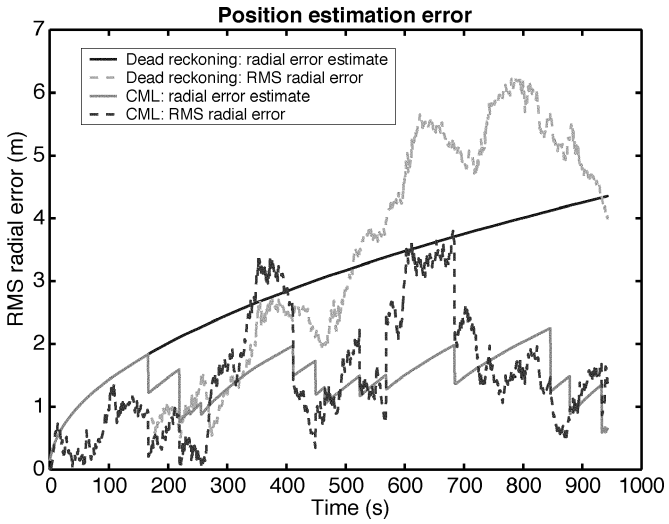

Fig. 4. Concurrent mapping and localization. The radial position error and the corresponding estimate, obtained from the covariance matrix terms for the CML solution, grow until the landmarks are reobserved. When these events occur, the sensor position error decreases. The error then grows again until another landmark is reobserved. The navigation radial position error and the estimated radial error for the dead-reckoning solution keep growing without bounds.

where θ_v is the heading of the vehicle with respect to the world frame and $\bar{x}_i$, $\bar{y}_i$ are, respectively

$$\bar{x}_i = x_i - x_v \tag{8}$$

$$\bar{y}_i = y_i - y_v. \tag{9}$$

The coordinates with respect to the world frame of landmark i and of the vehicle are $[x_i\ y_i]$ and $[x_v\ y_v]$, respectively.

The equation for initializing a new landmark is

$$\mathbf{x_{n+1}} = \begin{bmatrix} x_v + r\sin(\psi + \theta_v) \\ y_v + r\cos(\psi + \theta_v) \end{bmatrix} \tag{10}$$

A vehicle using a sidescan sonar will return range to the landmark and the observation vector will be

$$\mathbf{z_i} = \begin{bmatrix} \sqrt{r^2 - h^2} \\ h\sin(\phi) \end{bmatrix} \tag{11}$$

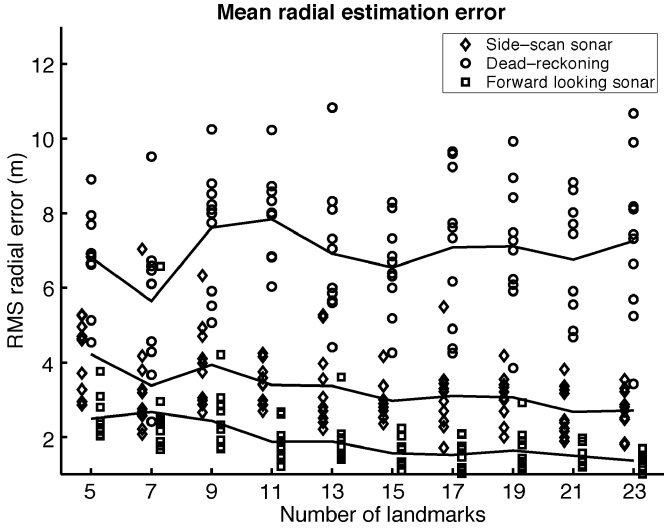

Fig. 5. Mean radial-estimation error. One point is plotted per simulation. CML improves the estimate obtained by dead reckoning. The forward-look sonar demonstrates the best performance.

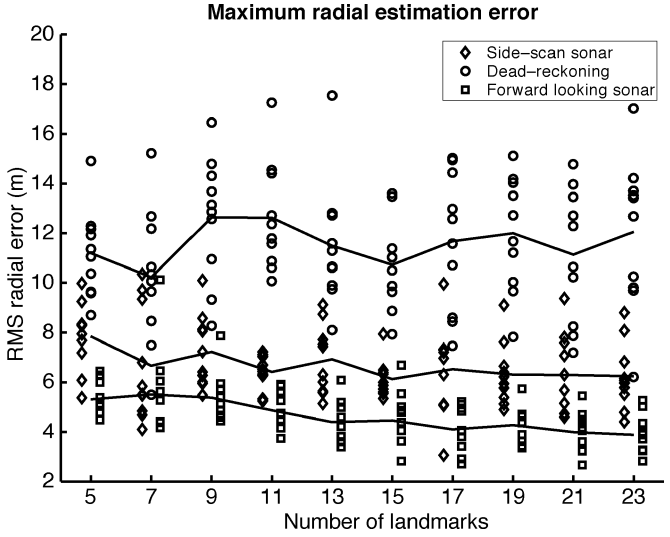

Fig. 6. Maximum radial-estimation error. The maximum radial error at any point in the trajectory is plotted for each simulation. Sonar-based CML again outperforms the dead-reckoning solution and, again, the forward-look sonar performs the best.

where the cross-track distance is computed from the range r to the target and the height h to the sea floor and the along-track distance is computed from the height h to the sea floor and the pitch ϕ. The prediction of the target observation will be

$$\hat{\mathbf{z}}_\mathbf{i} = R_v \bar{\mathbf{x}}_\mathbf{i} \tag{12}$$

where R_v is a rotation matrix defined as

$$R_v = \begin{bmatrix} \cos\theta_v & -\sin\theta_v \\ \sin\theta_v & \cos\theta_v \end{bmatrix}. \tag{13}$$

New landmarks will be initialized, given

$$\mathbf{x}_{\mathbf{n+1}} = \mathbf{x}_\mathbf{v} + R_v^{-1}\mathbf{z}_\mathbf{i}. \tag{14}$$

C. Simulations

To evaluate the efficiency of CML, a simulator has been developed. A trajectory is generated. Compass and DVL measures are generated with bias noise for the compass and scale-factor errors for the DVL. The starting point coordinates (0,0) are assumed to be known. Landmarks are randomly spread in the area covered during the mission. The occurring time of observations are computed according to the sonar characteristics. The observation vectors are generated with noise. The DVL is assumed to have a 0.5% scale factor error and is affected by a 0.1 m/s $- 1\sigma$ white noise. The compass is assumed to have a 0.2° bias and is affected by a $1.5^\circ - 1\sigma$ white noise. They both provide measurements at 1 Hz. Noise on the forward-look sonar has been taken into account and modeled as 0.1 m $- 1\sigma$ on range and $0.5^\circ - 1\sigma$ on bearing. The sidescan sonar measured distances have 0.05 m $- 1\sigma$ cross-track noise. As pitch is not measured on all UUVs, noise corresponding to a maximum pitch of 4.5° at 10 m of altitude has been simulated. The simulator assumes that the sidescan sonar cannot observe anything over a predetermined yaw rate. The range of the forward-look sonar is 75 m with a 90° field of view and provides images at 1 Hz. The sidescan sonar is a two-side system with no blind-range zone. The range for both sides is 30 m in order to provide high-resolution images for the mission needs. The data association is perfect; there are no mismatches between landmarks.

1) Behavior of CML Using Sidescan Sonar: Figs. 3 and 4 show the results of a simulation. With only two observations for seven of the landmarks and three observations for the three remaining landmarks, the stochastic map algorithm yields satisfactory position estimation and landmark localization. The final estimate has a 1.4-m error, whereas the drift in the dead-reckoning navigation was 3.99 m. The worst-position estimate has been reduced from 6.25 m down to 3.81 m. The localization of the landmarks is achieved with a mean radial estimated error of 1 m and a maximum estimated radial error of 2 m, derived from the stochastic map's covariance matrix. The estimated error is shown to evolve in a manner similar to the actual radial error and can be considered to be a suitable approximation. The algorithm's behavior is very close to the one predicted by the theorems expressed in [36]. In a set workspace, the root-mean-square (rms) error is well bounded. The algorithm seems to be robust to nonmodeled scale-factor errors and bias noise.

2) Comparison Between Sidescan Sonar and Forward-Look Sonar CML: The efficiency of CML using sidescan sonar has been compared with CML using forward-look sonar and dead-reckoning estimation performed by a Kalman filter for different landmark densities. Both sonars are tested on the same set of data for each simulation. Ten simulations are run per landmark density setting. The mission scenario covers a 500×200 m^2 area. The sonars follow a trajectory of 20 parallel and equally spaced linear tracks that cover all the mission space; they then return to the starting point.

The data association is assumed to be perfect for both sonars; whereas this assumption is reasonable for sidescan sonar, it is optimistic for the forward-look sonar. Using a forward-look sonar, multiple instances of the same landmarks are likely to be stored in the map [18], thus reducing the efficiency of the filter.

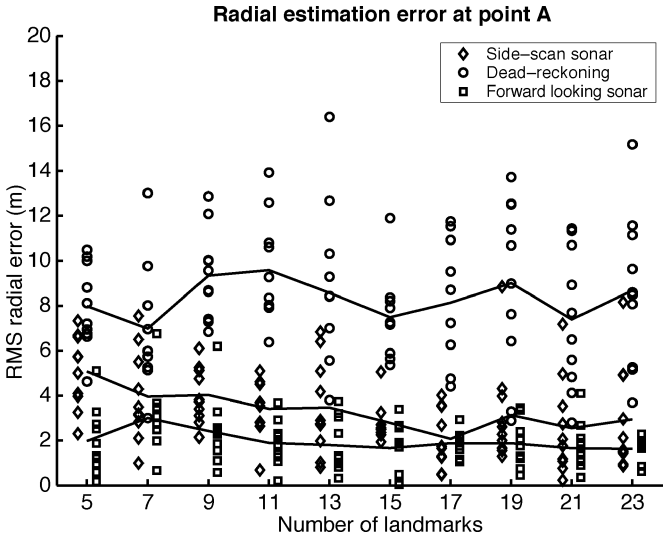

Fig. 7. Last-track trajectory error. The error when the vehicle reaches the last track trajectory, and just before it returns to the starting point, is again smaller for the CML solutions. The forward-look sonar marginally offers the best performance.

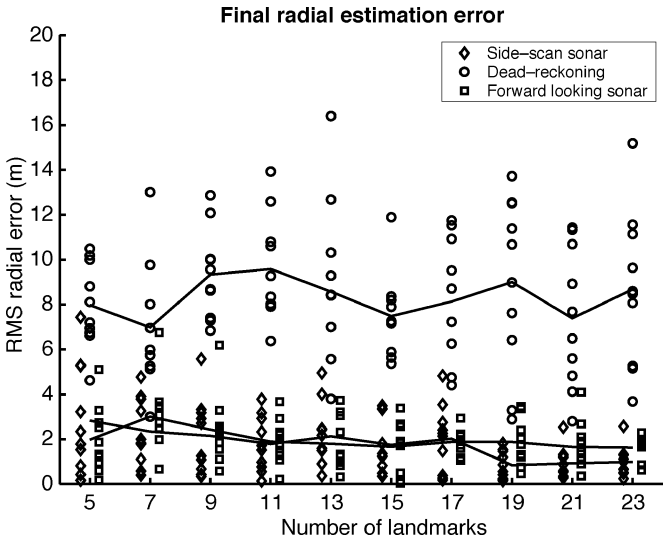

Fig. 8. End-of-mission error. The error when the vehicle has finished the mission and returns to the start point is comparable for both the sidescan and forward-look sonar.

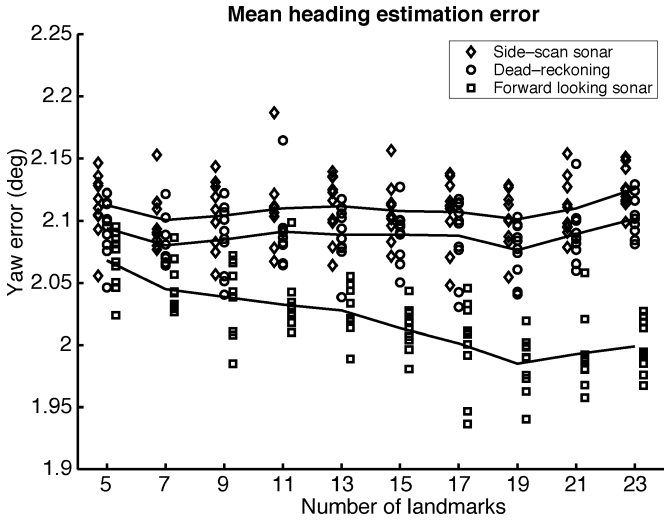

Fig. 9. Mean-heading error. The choice of sonar for CML has an impact on the heading estimation. The sidescan degrades its estimation and the forward-look sonar improves it, especially with a high landmark density.

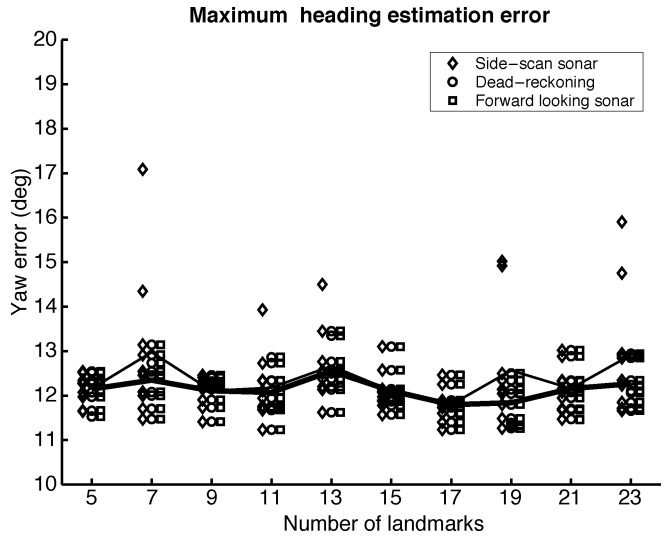

Fig. 10. Maximum-heading error. The maximum-heading error at any one point in the trajectory for all the simulations, although considerable, remains similar for all three processes.

The sidescan will generally observe a third of the landmarks twice; the rest of the landmarks will be observed three times.

On average, the forward-look sonar performs 23 times more observations per landmark than the sidescan sonar does. Given this number, results presented in Figs. 5 and 6 are not surprising. These figures are the mean and maximum position errors for all the missions and landmark distributions ranging from 5 to 23. According to the values depicted in these figures, CML using a forward-look sonar is, on average, approximately two times better than CML using a sidescan sonar at estimating the vehicle's position.

Fig. 7 illustrates the error when the vehicle reaches the last track in the set; at this point, the vehicle is ready to return to the starting point and finish the mission. This figure shows that both sonars are successful in creating and updating a stochastic map. However, between two observations the error of the sidescan sonar stochastic map grows. The forward-look sonar, on the other hand, continues to track landmarks due to its higher rate of observations. The error growth for the forward-look sonar is, thus, limited in comparison.

When the vehicle finally reaches its last waypoint, the landmarks mapped at the beginning of the mission are reobserved. The vehicle error at this point is bounded by the observation of these landmarks. The localization solutions at this stage of both the forward-look sonar and the sidescan sonar are comparable (see Fig. 8).

The accuracy of CML using sidescan sonar is more dependent on the landmarks' distribution. For the four criteria used above, their standard deviation is between one-and-a-half and two times higher with sidescan sonar than with forward-look sonar.

Figs. 9 and 10 show the mean and maximum errors in the heading estimates. The lack of accuracy of the three processes

is due to the centrilinear dynamic model, which assumes a constant heading; this leads to high errors in the turns. Observations of landmarks around a turn with the forward-look sonar provide extra information. For the sidescan, without a pitch sensor, the along-track distance between the landmark and the vehicle is pure noise. With such a sensor, accuracy on both position and yaw will be improved.

III. Smoothing the Stochastic Map

The previous section demonstrated the effectiveness of CML using sidescan sonar to provide the vehicle with a position estimate in order to carry out its task. Observations, by correcting the drift, create jerks in the estimation. Thus, this trajectory estimation is unsuitable for some data-exploitation techniques, such as mosaicing. CML using sidescan sonar is less useful without an appropriate smoothing postprocess.

The *Rauch–Tung–Striebel (RTS)* backward filter is usually used to smooth the output of a Kalman filter [39]. The next section describes how the RTS works and Section III-B will introduce a solution capable of smoothing the stochastic map output with the RTS filter.

A. RTS Filter

Estimating is a real-time data-processing scheme that only uses the measurements between 0 and t to estimate the state of a system at a certain time t, where $0 \leq t \leq T$, while smoothing is a nonreal-time data-processing scheme that uses all measurements between 0 and T to do it. In the discrete time case, let us define k as $k = 1, 2, 3, \ldots, N$, where $k = t/s$ for sampling period s and $N = T/s$. In the discrete case, the scheme uses all measurements taken at discrete time periods from $k = 0$ to $k = N$

An optimal smoother can be thought of as a suitable combination of two optimal filters. One of the filters, called a "forward filter," operates on all the data before time t and produces the estimate $\hat{\mathbf{x}}_f$. The other filter, called a "backward filter," operates on all the data after time t and produces the estimate $\hat{\mathbf{x}}_b$. Together, these two filters use all the available information. The optimal smoother is sought in the form

$$\hat{\mathbf{x}} = A\hat{\mathbf{x}}_f + B\hat{\mathbf{x}}_b. \tag{15}$$

Optimization of (15) leads to the optimal smoother

$$\begin{cases} \hat{\mathbf{x}} = \mathbf{P}\left(\mathbf{P}_f^{-1}\hat{\mathbf{x}}_f + \mathbf{P}_b^{-1}\hat{\mathbf{x}}_b\right) \\ \mathbf{P}^{-1} = \mathbf{P}_f^{-1} + \mathbf{P}_b^{-1} \end{cases} \tag{16}$$

where $\mathbf{P}$, $\mathbf{P}_f$, and $\mathbf{P}_b$ are, respectively, the error covariance of the smoothed estimate, that of the forward estimate, and that of the backward estimate. A state is said to be smoothable if an optimal smoother provides a state estimate superior to the one obtained when the final estimation of the optimal filter is extrapolated backward in time.

At time T, the estimate of the forward filter uses all the available information, so $\mathbf{P} = \mathbf{P}_f$. This leads to the boundary condition for $\mathbf{P}_b : \mathbf{P}_b^{-1}(T) = 0$. This is a major issue for initializing the backward filter, which is circumvented by developing the backward filter propagation equation and the smoother equation to find an equivalent form: the RTS form. This form does not involve the backward filter per se; the forward Kalman filter is run first. Then, its last estimate and covariance are used to initialize the smoothed estimate, which is obtained by running the backward RTS equations. For linear systems

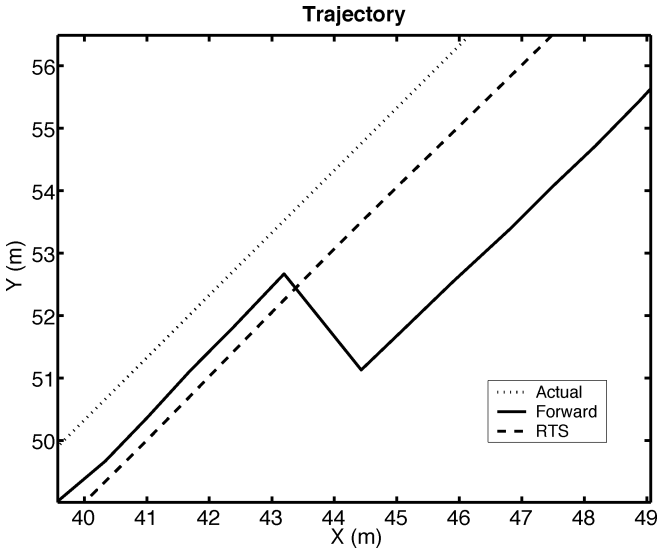

Fig. 11. Results using smoother. Running the RTS on the vehicle state produces a smoothed estimate. Zooming on the trajectory estimation shows how the RTS trajectory experiences no jerks when the state is corrected after reobserving a landmark. The forward estimate, on the other hand, does experience a jerk.

$$\begin{aligned} \hat{\mathbf{x}}(k|N) &= \hat{\mathbf{x}}_f(k|k) + \mathbf{A}(k)\left[\hat{\mathbf{x}}(k+1|N) - \hat{\mathbf{x}}_f(k+1|k)\right] \\ \mathbf{A}(k) &= \mathbf{P}_f(k|k)\mathbf{F}'\mathbf{P}_f(k+1|k)^{-1} \\ \mathbf{P}(k|N) &= \mathbf{P}_f(k|k) + \mathbf{A}(k) \\ &\quad \times \left[\mathbf{P}(k+1|N) - \mathbf{P}_f(k+1|k)\right]\mathbf{A}(k)' \end{aligned} \tag{17}$$

where $\hat{\mathbf{x}}_f(k|k)$ and $\hat{\mathbf{x}}_f(k+1|k)$ denote the prediction and correction states of the forward filter at instant k and $\mathbf{P}_f(k|k)$ and $\mathbf{P}_f(k+1|k)$ are their respective covariances. At time instant k, the smoothed estimate is $\hat{\mathbf{x}}(k|N)$ and $\mathbf{P}(k|N)$ is its error covariance. The transition matrix for the system is $\mathbf{F}$. As is the case for the EKF, a first-order approximation of the nonlinearities can be made to account for these. The equation remains unchanged, but for the transition matrix $\mathbf{F}$, which is now substituted by $\mathbf{J}_{\mathbf{x}}(k|k)$, the Jacobian of the process (vehicle) model with respect to the state evaluated at $\hat{\mathbf{x}}_f(k|k)$.

B. Smoothing the Stochastic Map Output

The stochastic map is not of a fixed size. As new observations are made, the state and associated covariance increase in size to accommodate them. The RTS was not designed to operate under these circumstances; it must operate on matrices and vectors of constant sizes. The strategy is to increase the size of all the stored states and vectors to match the final size of the stochastic map. The values of the landmark states and covariances before the first observation of these is performed must also be decided. Fixing the values to zeros will cause a numerical instability. The obvious choice is to make them equivalent to the output of the filter after the first observation of that landmark. That is to say,

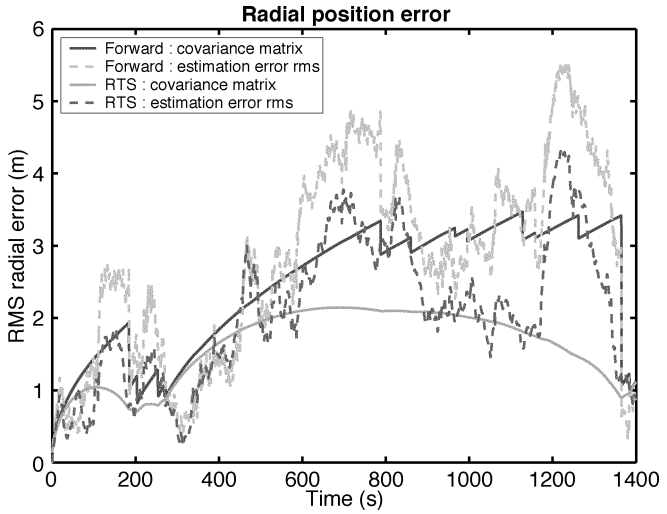

Fig. 12. The rms position error. The improved RTS filter accuracy can be confirmed by observing the rms error with respect to the true (simulated) trajectory. The true error of both the stochastic map and the RTS filter solutions closely follow their respective $1-\sigma$ covariance estimates. The rms and covariance errors for the stochastic map solutions grow until the landmarks are reobserved; at this stage, the errors drop. The new error values are a function of the landmarks' positions errors, the errors of the observations, and the vehicle's position errors when the observations take place. The rms and covariance errors for the RTS filter solution are smaller, as the filter now uses the forward and backward estimates. The errors also drop when the landmarks are reobserved. This is more apparent as the first three and last landmarks are reobserved.

the position of that landmark before it was observed must have been the same as it was after it was observed and this is as certain before as it was after. The correlations terms to other landmarks and to the vehicle before the landmark was observed are set to zero, because only after it has been observed can the landmark be correlated to the rest of the workspace.

The RTS filter is implemented on the forward-state estimation obtained by the CML. Figs. 11 and 12 show the results from the simulation. The RTS estimate is smooth: no jerks can be observed. The covariance matrix is also smooth and significantly smaller than the forward covariance matrix and the position error is reduced. For ten simulations, the mean rms errors with RTS were 0.76 times the mean rms errors without RTS. The mean heading rms errors with RTS were 0.73 times the mean heading rms errors without rms. The accuracy improvement is not as spectacular as is suggested by the covariance matrix, although no simulation has shown an increase of the estimation error and the result is always smooth.

The next section shows results obtained with real data, which show how the smoothed CML output can be used to create very high-quality mosaics.

IV. Results with Real Data

The following results were obtained by processing data gathered during the BP'02 experiments carried out by the Supreme Allied Commander Atlantic (SACLANT) Undersea Research Centre, La Spezia, Italy. The sidescan data was gathered by a REMUS AUV [4]; its position output consists of a synchronous stream of data updated every second. The data stream outputs the AUV's speed and heading, as well as a processed navigation solution. The AUV uses acoustic transponders to compute this

TABLE I
Kalman Filter and Stochastic Map Errors

Initial Estimated Position Error (m):	300
Initial Estimated Heading Error (°):	90
Initial Estimated Speed Error (m/s):	10
Measurement LBL Position Error (m):	60
Measurement Heading Error (°):	10
Measurement Speed Error (m/s):	0.05
Side-scan Range Error (m):	1
Process Heading Error (°):	10
Process Speed Error (m/s):	1

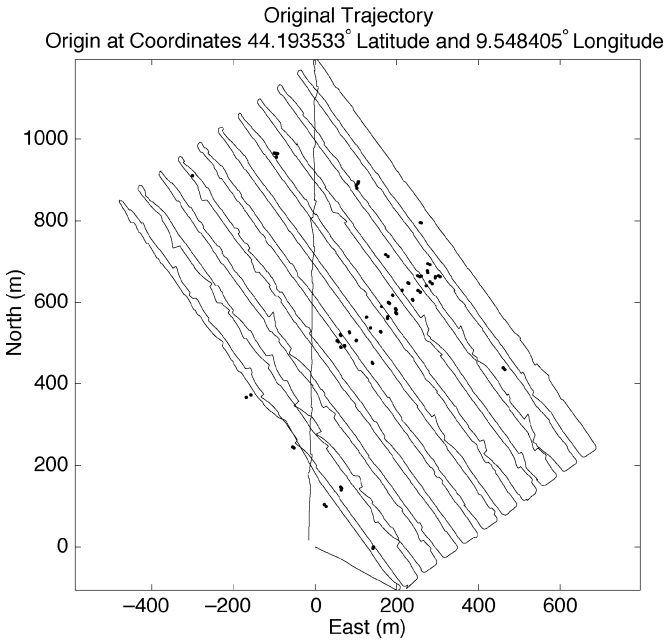

Fig. 13. Original REMUS trajectory. The output trajectory for the REMUS mission starts at the origin. The position of the observations and reobservations of the 43 landmarks has been superimposed to the original trajectory. This diagram shows the spatial distribution of these landmarks. Note how there are only six observations and corresponding reobservations at the beginning of the mission on the first two tracks. There are no observations from the third track until the seventh and eighth tracks, when one landmark is observed and reobserved. The observations do not become commonplace until the ninth track. There are no observations after the vehicle reaches the last waypoint, at approximate coordinates 0 (m) east and 1195 (m) north, as it returns toward the mission start point.

solution. The output from the fixes is not given in the REMUS data stream; therefore, the authors had to derive these position updates from the data, which was necessary as the output would be used as the input to a Kalman filter and also to the CML system. To derive these updates, the authors developed an algorithm that, given a considerable change in position (a change outside of the predicted position), would extract the new position of the vehicle and assume it to be an update from the acoustic transponders. The changes had to be considerable in order to distinguish between vehicle maneuvers and acoustic transponder updates. The method ensures that only outputs from the transponders are extracted. Unfortunately, this means that in cases where the dead reckoning and acoustic transponders produce a similar result, the transponder output will be ignored.

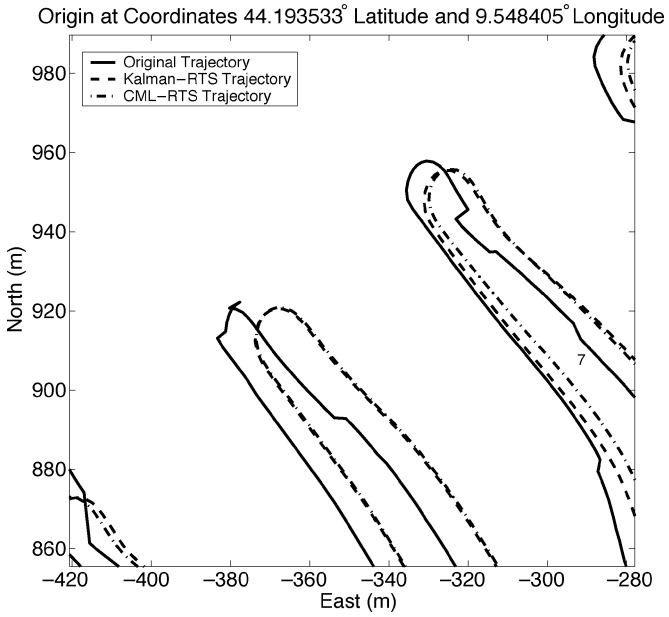

Fig. 14. All trajectories. The original trajectory, the Kalman–RTS trajectory, and the CML–RTS trajectory can all be compared. The Kalman–RTS and CML–RTS trajectories both correct the navigation before and after the LBL fixes. Only the CML–RTS trajectory corrects the trajectories when landmarks are observed. In this section of the mission, the CML–RTS trajectory is corrected by the observation of landmark 7.

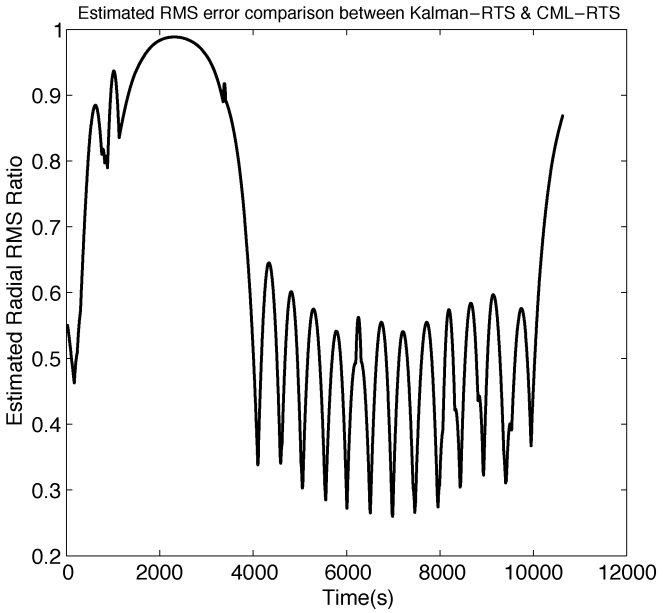

Fig. 15. Ratio of estimated rms radial errors. The estimated CML–RTS filter is more accurate than the Kalman–RTS filter; these errors are obtained using the stored covariances. The ratio is smaller at the start of the mission as landmark observations help to bring the CML-RTS error down. The lack of landmarks through the third to sixth tracks in the trajectory results in the estimated error ratio being close to one. On the rest of the tracks, the higher density of landmarks results in the better performance of the CML–RTS solution, close to three times better when the landmarks are reobserved and two times better between reobservations. At the end of the mission, there are no further reobservations and, again, the performance of the CML–RTS filter tends to that of the Kalman–RTS filter.

The REMUS data was used to run both a Kalman–RTS and a CML–RTS system. Table I lists the errors chosen for each of the Kalman and stochastic map parameters. These values are larger than the values quoted by sensor manufacturers; the intention is to produce a consistent solution despite possible errors that might be introduced when manipulating the data to extract the possible LBL position updates.

Unlike the simulations in this real mission, the AUV is also aided by LBL fixes. The Kalman–RTS and CML–RTS also use these fixes in these experiments. The results obtained and detailed below suggest that the Kalman–RTS provides better accuracy than the original trajectory. The CML–RTS provides better accuracy and better visual mosaics than both the Kalman–RTS and the original trajectory. Thus, the CML strategy is able to also work alongside absolute sensors.

The sonar data from the REMUS was used to manually extract landmarks. Some error might have been introduced in the process of manually extracting the landmarks to produce the observation vectors (11). These landmarks were also associated to each other manually and the associations were perfect; there were no mismatches. The sonar images are time stamped and can be referred to for navigation.

The mission examined in this paper lasted 2 h, 57 min, and 8 s. The REMUS navigation output for the mission (Fig. 13) was processed and used to create Kalman–RTS and CML–RTS solutions. A section of the workspace showing part of the solutions and the original navigation output from the REMUS can be seen in Fig. 14. The results show that the RTS solutions are smoother and also are able to correct the navigation before and after the LBL fixes. The results also show that the Kalman–RTS and CML–RTS trajectories are different; this difference results from the inclusion of the landmarks' observations in the CML–RTS solution. Consequently, the estimated radial RMS error, obtained from the stored covariance information, for the CML–RTS trajectory is of smaller magnitude than the Kalman–RTS trajectory. The ratio of the estimated CML–RTS radial error over the estimated Kalman–RTS radial error is, on average, 0.635. Fig. 15 shows the evolution of this ratio for the whole mission. Close inspection of this figure reveals that the CML–RTS solution is estimated to be more accurate throughout. The CML–RTS solution is approximately three times more accurate where landmarks are observed and reobserved.

The mismatch errors between the observed landmarks' positions were extracted for the original trajectory, the Kalman–RTS trajectory, and the CML–RTS trajectory. The positions were obtained by georeferencing the landmarks' observations using the appropriate trajectory and observation parameters. The errors were obtained by finding the rms distance between matching landmarks' observations. Table II shows the maximum, minimum, and average rms errors obtained for each trajectory type. These errors show that the CML–RTS should be able to render higher quality georeferenced mosaics. The maximum error of 168.2 m for the original trajectory is a result of a landmark being observed before any LBL fixes take place, which suggests that the initial error in the vehicle position is close to that figure. The average rms error of 6.7 m, displayed by the Kalman–RTS trajectory, also suggest that the assumption that the LBL fixes have an accuracy of 60 m is likely to

TABLE II
LANDMARKS POSITIONS' MISMATCH RMS ERRORS

	Original Trajectory	Kalman-RTS Trajectory	CML-RTS Trajectory
Maximum Error (m)	168.2	21.1	2.2
Minimum Error (m)	1	0.8	0.0
Average Error (m)	26.7	6.7	0.8

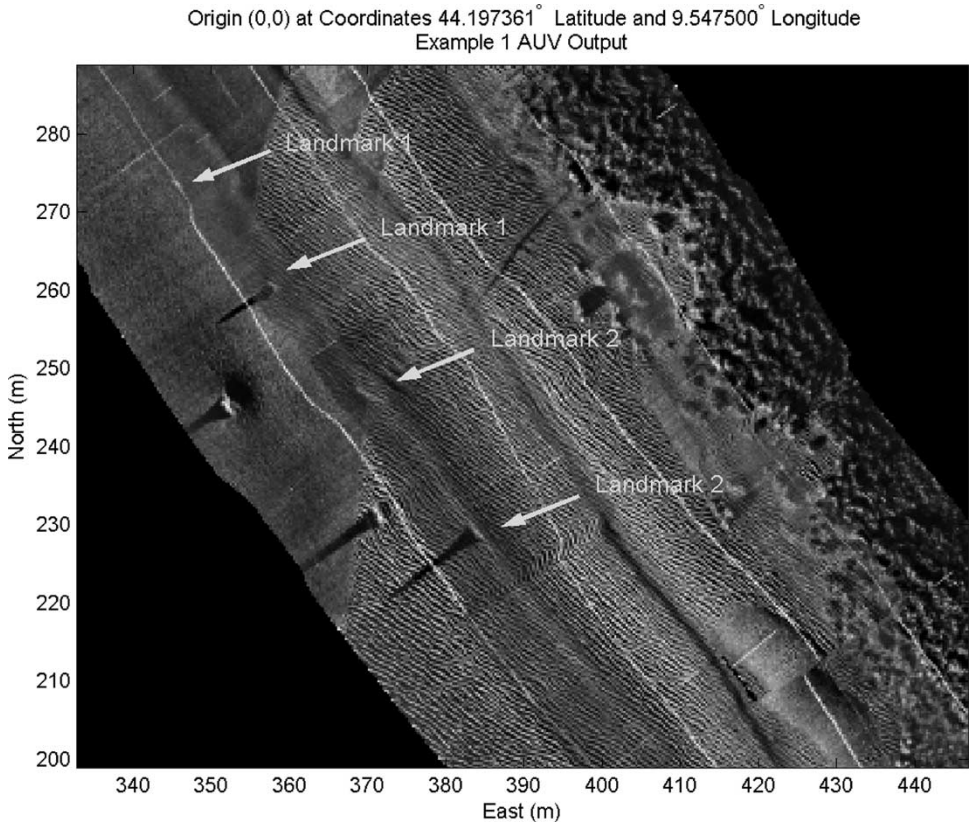

Fig. 16. Example 1: AUV output. This output is not smooth: Observe the jerks of the high-intensity surface returns (the thin white line following the vehicle track). The boundary formed by the sand-ripple region does not run smoothly across the image.

be very conservative. The difference in the average rms error between the Kalman–RTS and CML–RTS trajectories shows the real value of the CML–RTS solution.

The mosaics were produced by using the REMUS AUV navigation output, the Kalman–RTS output, and the CML–RTS output. From these, it is clear that the sidescan sonar mosaics, computed with the CML–RTS solution, offer the highest visual quality.

In the first example (Figs. 16–18), the images zoom into a large-scale mosaic of two overlapping REMUS tracks along the set of regularly spaced and parallel linear tracks. It is clear that the use of the Kalman–RTS output has helped to smooth the data. However, the errors between the landmarks are still persistent. On the other hand, the CML–RTS solution helps, not only in producing a smooth navigation output, but also in producing a visually coherent result. The landmarks and the features in the surrounding environment now fit together better.

The second example, shown in Figs. 19–21, is quite interesting. In this example, again of two overlapping tracks, the shadows created by the object can be seen to oppose each other as the object is seen from two different sides. This can be seen in Figs. 19 and 20, where the error in the landmark position illustrates the phenomenon. The resulting mosaic using the CML–RTS solution produces a view of the object with two distinct shadows. Shadows from objects are commonly used in object-detection algorithms; thus, the observed phenomenon might prove to be a useful tool in the future.

The third and final example shows the benefits of the Kalman–RTS solution over the AUV output. The AUV's dead reckoning is sometimes inaccurate. In these instances, an acoustic update will appear as a jerk in the trajectory. The error in the landmark position in these cases can be, in the worst cases, hundreds of meters. This is apparent in Fig. 22, where another two overlapping tracks are shown. The smoother improves the accuracy of the solution by using the knowledge gathered after the update and it produces a feasible output, as can be seen in Fig. 23. In any case, best results are again obtained when using the CML–RTS solution (Fig. 24).

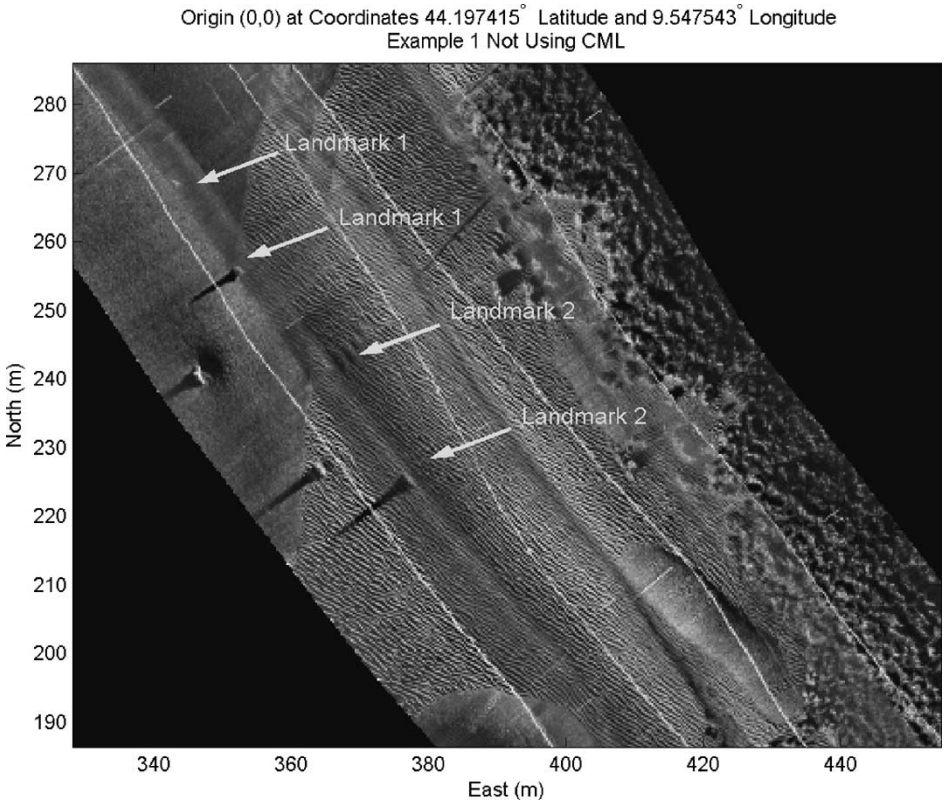

Fig. 17. Example 1: Not using CML. In this case, the navigation errors are not completely fixed. The smooth output can be seen by observing the surface returns (the thin white line following the vehicle track). The boundary formed by the sand ripples does not run smoothly across the image.

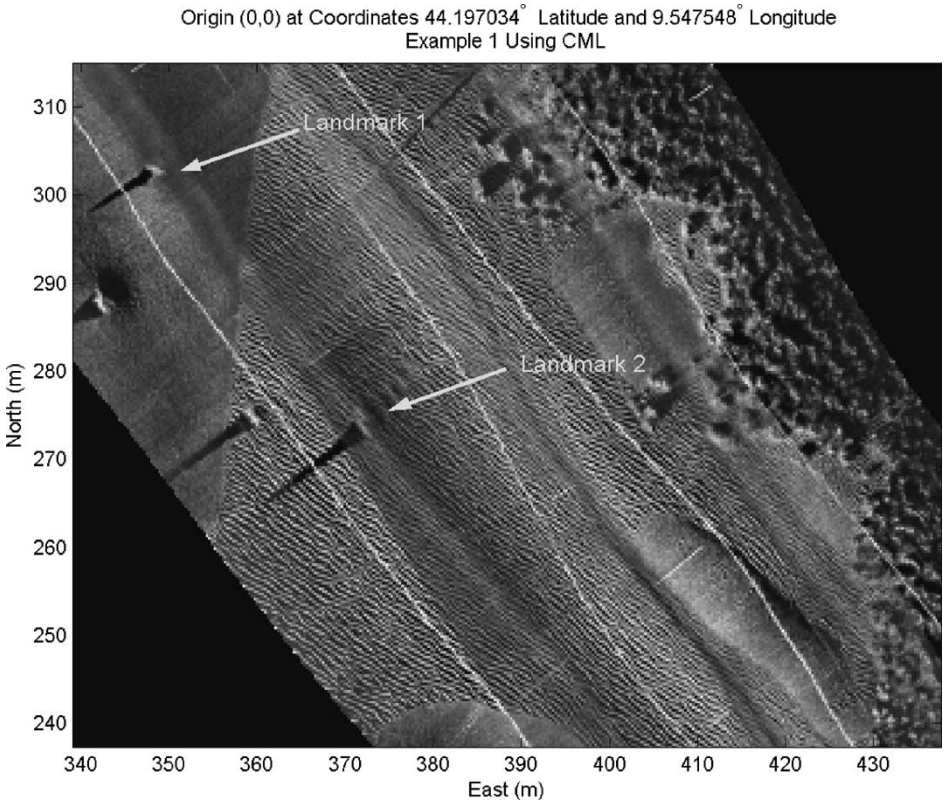

Fig. 18. Example 1: Using CML. The CML–RTS solution produces an accurate and smooth output: observe how the sand ripples form a single smooth boundary.

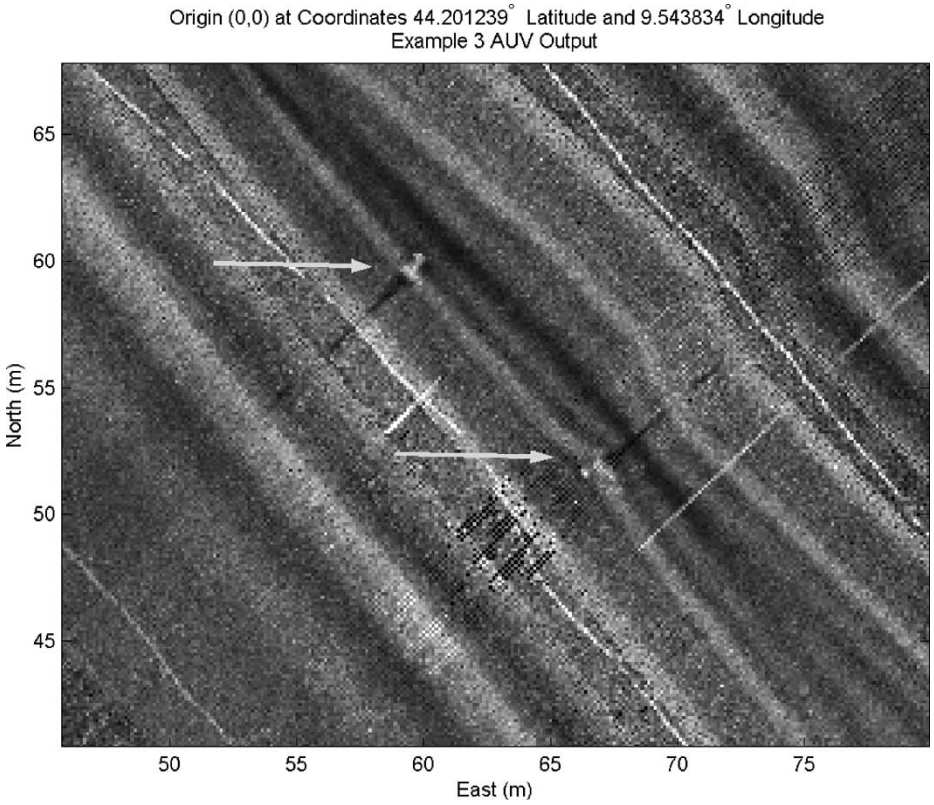

Fig. 19. Example 2: AUV output. In this example, the error is apparent by observing that the same landmark appear in two different locations. In the image, the gray stripes are caused by the geometry of the sidescan beams and their sidelobes. The thin white line following the vehicle track is caused by the surface returns.

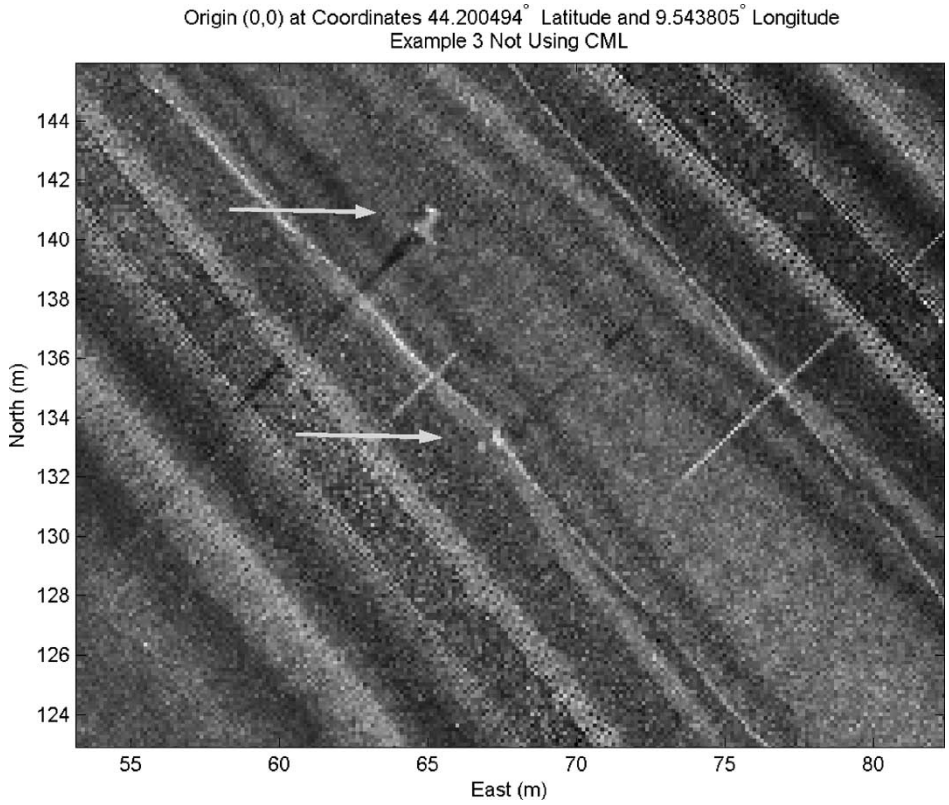

Fig. 20. Example 2: Not using CML. The landmark-positioning error persists when the trajectory is simply smoothed using a Kalman–RTS algorithm.

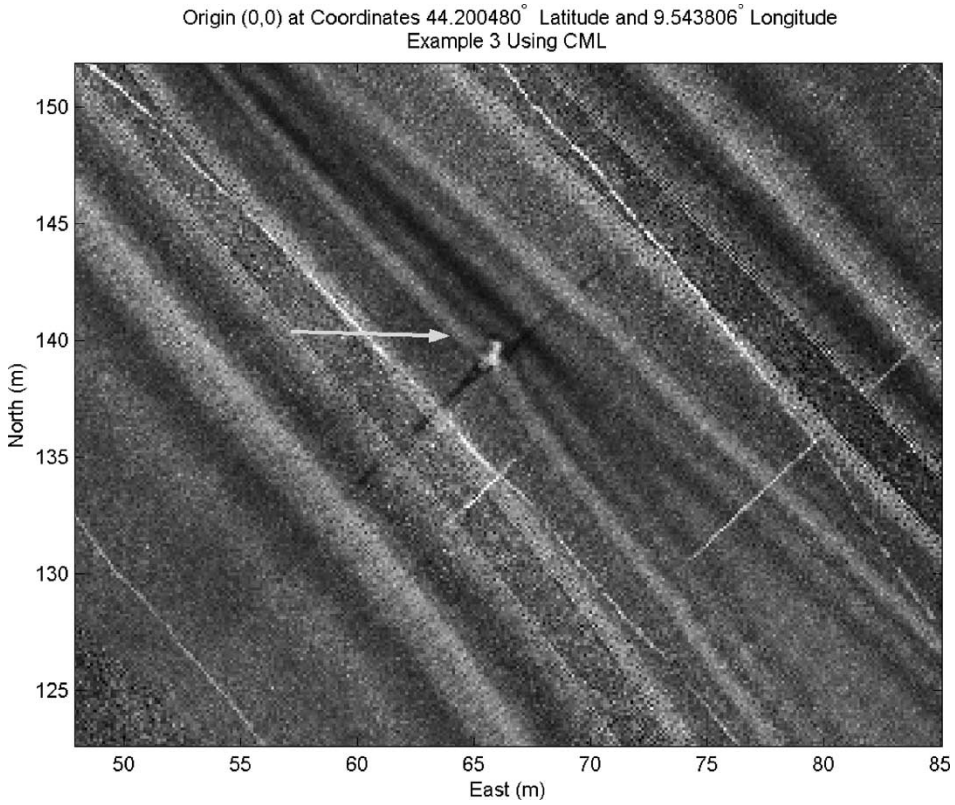

Fig. 21. Example 2: Using CML. The CML–RTS solution corrects the relative navigation and the resulting mosaic displays a single landmark.

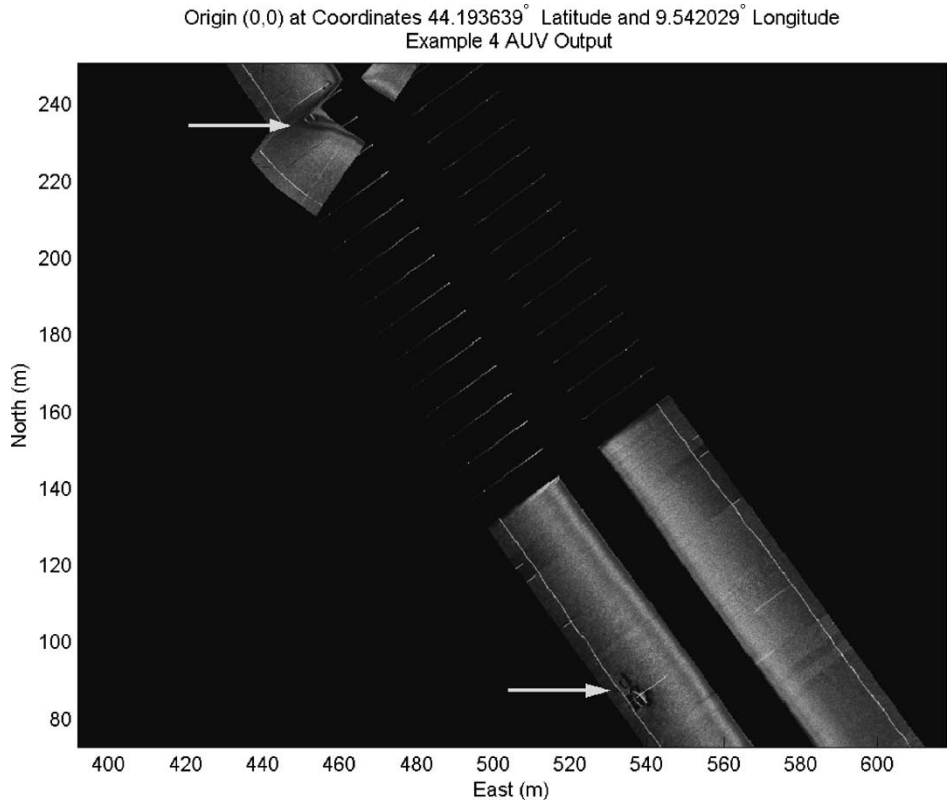

Fig. 22. Example 3: AUV output. The AUV error before it receives a fix from the acoustic transponders is considerable. In this case, it is more than 100 m.

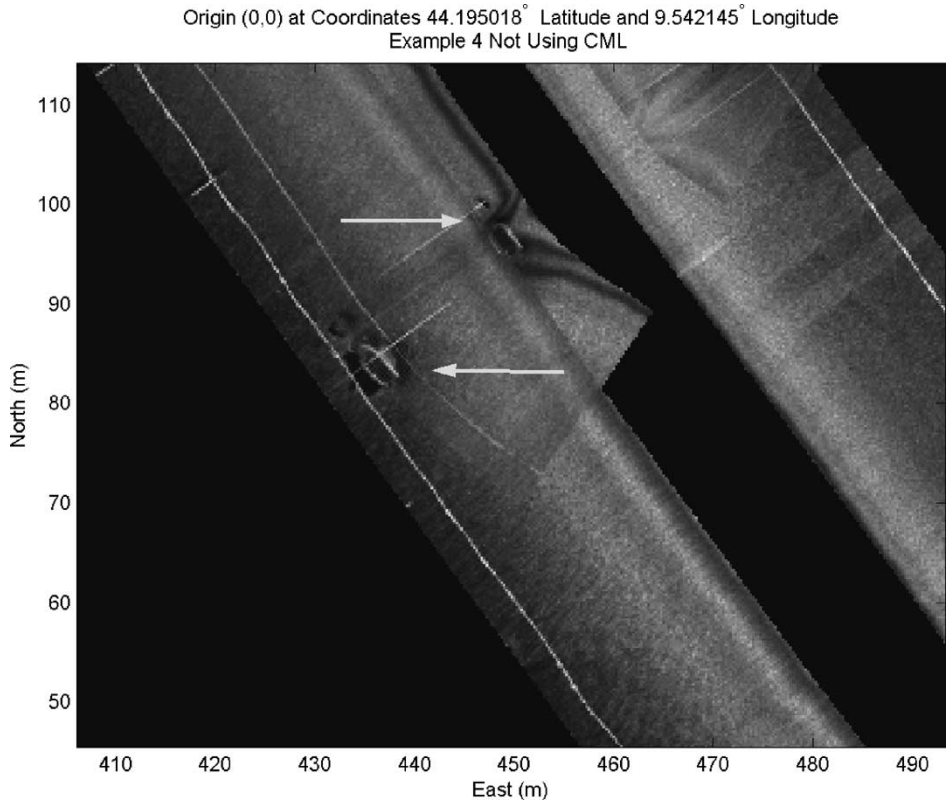

Fig. 23. Example 3: Not using CML. The Kalman–RTS strategy can be used to propagate the acoustic fix to points that occur in the trajectory before the fix.

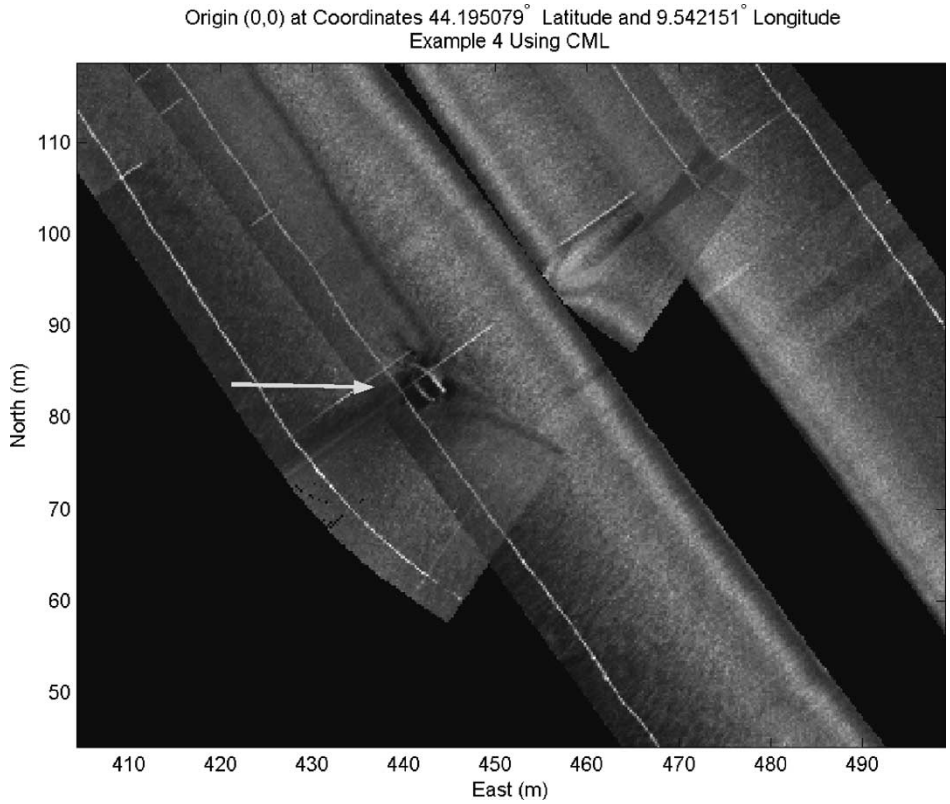

Fig. 24. Example 3: Using CML. The CML–RTS solution propagates the acoustic fix to points that occur in the trajectory before the fix and also corrects the trajectory to align the observed landmark.

V. Conclusion

For an AUV conducting a sidescan survey of the sea floor in overlapping parallel tracks, this paper has shown how uncertainty in estimates of its trajectory can be reduced with a CML–RTS algorithm implemented on sidescan images containing operator–identified perfectly matched targets.

Simulation results showed that CML using a sidescan sonar produces comparable solutions to a forward-look sonar system if landmarks stored at the beginning of a mission are reobserved. Simulations also showed that the mean rms error with CML–RTS using sidescan were 0.76 times the mean rms error of a forward CML without RTS smoothing.

Results with real data showed that the estimated error of the CML–RTS solution is, on average, 0.635 times the estimated error for the Kalman–RTS solution. Missmatch errors of multiple georeferenced landmark observations showed that, on average, the Kalman–RTS solution has an error of 6.7 m; the average error of the CML–RTS solution is 0.8 m.

In the future, the authors plan to include existing object-detection techniques [26], [40] and automatic data-association strategies [18] to simplify and minimize the operator's task of manually interpreting and matching the data.

Acknowledgment

The authors would like to thank the SACLANT Undersea Research Centre, the U.S. Office of Naval Research, and The Woods Hole Oceanographic Institution, Woods Hole, MA, for allowing the inclusion of data from the BP'02 experiment.

References

[1] J. Leonard and H. Durrant-Whyte, *Directed Sonar Sensing for Mobile Robot Navigation*. Norwell, MA: Kluwer, 1992.

[2] G. Grenon, P. E. An, S. M. Smith, and A. J. Healey, "Enhancement of the inertial navigation system for the morpheus autonomous underwater vehicles," *IEEE J. Oceanic Eng.*, vol. 26, pp. 548–560, Oct. 2001.

[3] D. B. Marco and A. J. Healey, "Command, control, and navigation experimental results with the nps aries auv," *IEEE J. Oceanic Eng.*, vol. 26, pp. 466–476, Oct. 2001.

[4] C. von Alt, B. Allen, T. Austin, N. Forrester, R. Goldsborough, M. Purcell, and R. Stokey, "Hunting for mines with REMUS: A high performance, affordable, free swimming underwater robot," in *Proc. MTS/IEEE Int. Conf. OCEANS'01*, 2001, pp. 117–122.

[5] M. B. Larsen, "Autonomous navigation of underwater vehicles," Ph.D. dissertation, Dept. Automation, Tech. Univ. Denmark, Lyngby, Denmark, 2001.

[6] O. Bergem, "Bathymetric navigation of autonomous underwater vehicles using a multibeam sonar and a Kalman filter with relative measurement covariance matrices," Ph.D. dissertation, Univ. Trondheim, Trondheim, Norway, Dec. 1993.

[7] D. E. Di Massa, "Terrain-relative navigation for autonomous underwater vehicles," Ph.D. dissertation, Massachusetts Inst. Technol. (MIT), Cambridge, and Woods Hole Oceanogr. Inst., Woods Hole, MA, 1997.

[8] P. Newman and H. Durrant-Whyte, "Using sonar in terrain-aided underwater navigation," in *Proc. IEEE Int. Conf. Robotics Automation*, vol. 1, Leuven, Belgium, May 1998, pp. 440–445.

[9] M. Sistiaga, J. Opderbecke, and M. Aldon, "Depth image matching for underwater vehicle navigation," in *Proc. Int. Conf. Image Analysis Processing*, 1999, pp. 624–629.

[10] G. C. Bishop, "Gravitational field maps and navigational errors," *IEEE J. Oceanic Eng.*, vol. 27, pp. 726–737, July 2002.

[11] R. N. Carpenter, "Concurrent mapping and localization with FLS," in *Proc. Workshop Autonomous Underwater Vehicles*, Cambridge, MA, Aug. 1998, pp. 133–148.

[12] R. N. Carpenter and M. R. Medeiros, "Concurrent mapping and localization and map matching on autonomous underwater vehicles," in *Proc. MTS/IEEE Int. Conf. OCEANS'01*, 2001, pp. 380–389.

[13] J. J. Leonard and H. J. S. Feder, "Decoupled stochastic mapping," *IEEE J. Oceanic Eng.*, vol. 26, pp. 561–571, Oct. 2001.

[14] S. Negahdaripour and X. Xu, "Mosaic-based positioning and improved motion-estimation methods for automatic navigation of submersible vehicles," *IEEE J. Oceanic Eng.*, vol. 27, pp. 79–99, Jan. 2002.

[15] S. Thrun, D. Fox, and W. Burgard, "Probalistic mapping of an environment by a mobile robot," in *Proc. IEEE Int. Conf. Robotics Automation (ICRA'98)*, Leuven, Belgium, May 1998, pp. 1546–1551.

[16] J. Castellanos, J. Martinez, J. Neira, and J. Tardos, "Simultaneous map building and localization for mobile robots: A sensors fusion approach," in *Proc. IEEE Int. Conf. Robotics Automation (ICRA'98)*, Leuven, Belgium, May 1998, pp. 1244–1249.

[17] R. Smith, M. Self, and P. Cheeseman, "Estimating uncertain spatial relationships in robotics," in *Autonomous Robot Vehicles*, I. Cox and G. Wilfong, Eds. New York: Springer-Verlag, 1990.

[18] I. Tena Ruiz, "Enhanced concurrent mapping and localization using forward-looking sonar," Ph.D. dissertation, Heriot-Watt Univ., Edinburgh, U.K., Sept. 2001.

[19] P. Newman, "On the Structure and solution of the simultaneous localization and map building problem," Ph.D. dissertation, Univ. Sydney, Sydney, Australia, 1999.

[20] I. Tena Ruiz, Y. Petillot, and D. M. Lane, "AUV navigation using a forward looking sonar," in *Proc. Unmanned Underwater Vehicle Symposium*, Newport, RI, Apr. 2000.

[21] S. Reed, J. Bell, and Y. Petillot, "An unsupervised approach to the detection and extraction of mine features in side scan sonar," in *Proc. CAD/CAC 2001 Conf.*, Halifax, NS, Canada, Nov. 2001.

[22] I. Tena Ruiz, D. M. Lane, and M. J. Chantler, "A comparison of interframe feature measures for robust object classification in sector scan sonar image sequences," *IEEE J. Oceanic Eng.*, vol. 24, pp. 458–469, Oct. 1999.

[23] C. Bouman and M. Shapiro, "A multiscale random field model for Bayesian image segmentation," *IEEE Trans. Image Processing*, vol. 3, pp. 167–177, Mar. 1994.

[24] H. Derin and H. Elliot, "Modeling and segmentation of noisy and textured images using Gibbs random field," *IEEE Trans. Pattern Anal. Machine Intell.*, vol. PAMI-9, pp. 39–55, Jan. 1987.

[25] E. Trucco, Y. Petillot, I. Tena Ruiz, C. Plakas, and D. M. Lane, "Feature tracking in video and sonar subsea sequences with applications," *Comp. Vision Image Understanding*, vol. 79, pp. 92–122, 2000.

[26] S. Reed, J. Bell, and Y. Petillot, "Unsupervised segmentation of object shadow and highlight using statistical snakes," in *Proc. Generic Oceanographic Array Technology Systems (GOATS'00) Conf.*, La Spezia, Italy, Aug. 2001.

[27] C. M. Smith, "Integrating mapping and navigation," Ph.D. dissertation, Massachusetts Inst. Technol., Cambridge, MA, June 1998.

[28] T. Bailey, E. M. Nebot, J. K. Rosenblatt, and H. F. Durrant-Whyte, "Data association for mobile robot navigation: a graph theoretic approach," in *Proc. IEEE Int. Conf. Robotics Automation*, vol. 3, 2000, pp. 2512–2517.

[29] J. Neira and J. D. Tardós, "Robust and feasible data association for simultaneous localization and map building," in *Proc. IEEE Int. Conf. Robotics and Automation*, vol. Workshop W4, Mobile Robot Navigation and Mapping, San Francisco, CA, Apr. 2000.

[30] I. Tena Ruiz, Y. Petillot, D. M. Lane, and C. Salson, "Feature extraction and data association for AUV concurrent mapping and localization," in *Proc. IEEE Int. Conf. Robotics Automation (ICRA'01)*, Seoul, Korea, May 2001, pp. 2785–2790.

[31] J. Uhlmann, "Dynamic map building and localization: New theoretical foundations," Ph.D. dissertation, Univ. Oxford, Oxford, U.K., 1995.

[32] T. E. Fortmann, Y. Bar-Shalom, and M. Scheffe, "Sonar tracking of multiple targets using joint probabilistic data association," *IEEE J. Oceanic Eng.*, vol. OE-8, pp. 173–184, July 1983.

[33] S. Daniel, F. Le Leannec, C. Roux, B. Solaiman, and E. P. Maillard, "Side-scan sonar image matching," *IEEE J. Oceanic Eng.*, vol. 23, pp. 245–259, July 1998.

[34] P. Maybeck, *Stochastic Models, Estimation and Control*, ser. Mathematics in Science and Engineering. New York: Academic, 1982, vol. 141-2.

[35] Y. Bar-Shalom and T. Fortmann, *Tracking and Data Association*, ser. Mathematics in Science and Engineering. New York: Academic, 1988, vol. 179.

[36] M. W. M. G. Dissanayake, H. Durrant-Whyte, S. Clark, and M. Csorba, "A solution to the simultaneous localization and map building (SLAM) problem," Univ. Sydney, Sydney, Australia, Tech. Rep. ACFR-TR-01-99, Jan. 1999.
[37] J. A. Castellanos, J. D. Tardos, and C. Schmidt, "Building a global map of the environment of a mobile robot: The importance of correlations," in *Proc. IEEE Int. Conf. Robotics Automation*, Albuquerque, NM, Apr. 1997, pp. 1053–1059.
[38] M. W. M. G. Dissanayake, H. Durrant-Whyte, and T. Bailey, "A computationally efficient solution to the simultaneous localization and map building (SLAM) problem," in *Proc. IEEE Int. Conf. Robotics Automation*, San Francisco, CA, Apr. 2000, pp. 1009–1014.
[39] A. Gelb, Ed., *Applied Optimal Estimation*. Cambridge, MA: MIT Press, 1974.
[40] D. M. Lane, M. J. Chantler, and D. Y. Dai, "Robust tracking of multiple objects in sector scan sonar image sequences using optical flow motion estimation," *IEEE J. Oceanic Eng.*, vol. 23, pp. 31–46, Jan. 1998.

Ioseba Tena Ruiz (M'98) received the B.Eng (*Hons*) and Ph.D. degrees in electronic engineering from Heriot-Watt University, Edinburgh, U.K., in 1996 and 2001, respectively.

He has been with Heriot-Watt University as a Research Associate in five different research projects: CLASS (CMPT), ARAMIS (EU), AUTOTRACKER (EU), ALIVE (EU), and AMASON (EU). His research interests include navigation systems, concurrent mapping and localization, processing sonar returns, classifying sonar returns, and obstacle avoidance systems for autonomous underwater vehicles.

Sébastien de Raucourt received the M.S. degree in engineering sciences from Ecole Nationale Supérieure de Techniques Avancés (ENSTA; ParisTech), Paris, France, in 2002.

He was a Research Associate at Heriot-Watt University, Edinburgh, U.K., during his final-year placement. He helped to develop concurrent mapping and localization (CML) algorithms using sidescan sonar data. He has also been with Astrium, Toulouse, France, as an Attitude and Orbit Control Systems Engineer. His research interests include automatic control, signal processing, and navigation systems.

Yvan Petillot (M'03) received the Engineering degree in telecommunications with a specialization in image and signal processing, the M.Sc. degree in optics and signal processing, and the Ph.D. degree in real-time pattern recognition using optical processors from from the Université de Bretagne Occidentale, Ecole Nationale Supérieure des Télécommunications de Bretagne (ENSTBr), Brest, France,

He is a Specialist in sonar data processing (including obstacle avoidance) and sensor fusion. He has worked on various successful research projects in the field of image processing (such as ESPRIT III HICOPOS and MAST III ARAMIS) and currently is an Investigator for two European Union projects (FPV AMASON and AUTOTRACKER) and the Principal Investigator for two Engineering and Physical Sciences Research Council (EPSRC), U.K., projects (CRIME and CONSENSUS). He has developed an obstacle-avoidance system for autonomous underwater vehicles and is currently developing a classification system.

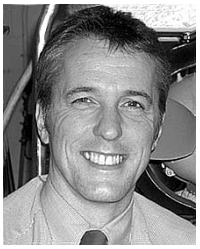

David M. Lane (M'92) received the B.Sc. degree in electrical and electronic engineering in 1980 and the Ph.D. degree for robotics work with unmanned underwater vehicles in 1986, both from Heriot-Watt University, Edinburgh, U.K.

He was a Visiting Professor with the Department of Ocean Engineering, Florida Atlantic University, Boca Raton, and is Cofounder/Director of See-Byte Ltd., Edinburgh, U.K. Previously, he was with the U.K. Defence and Offshore Industries. He currently is a Professor with the School of Engineering and Physical Sciences, Heriot-Watt University, Edinburgh, U.K., where he also is the Director of the University's Ocean Systems Laboratory. He leads a multidisciplinary team that partners with U.K., European and U.S. industrial and research groups supporting offshore, Navy, and marine science applications. Major sponsors include oil companies, the United States Navy, the European Union, and the U.K. Ministry of Defence. He has published over 150 journal and conference papers on tethered and autonomous underwater vehicles, subsea robotics, computer vision, image processing, and advanced control and is an Associate Editor for the *International Journal of Systems Science*.

Dr. Lane was the initial Chairman and Cofounder of the European MAROBOT special interest group on subsea robotics is a Member of Institution of Electrical Engineers (IEE), London, U.K., Professional Network on Robotics and the U.K. Society for Underwater Technology Underwater Robotics Committee. He is an Associate Editor of the IEEE JOURNAL OF OCEANIC ENGINEERING and regularly acts on program committees for IEEE Oceanic Engineering and Robotics and Automation Societies.